Biogeosciences Discuss., 9, 15127–15174, 2012
www.biogeosciences-discuss.net/9/15127/2012/
doi:10.5194/bgd-9-15127-2012

Biogeosciences Discussions

Technical Note: The Simple Diagnostic Photosynthesis and Respiration Model (SDPRM)

B. Badawy, C. Rödenbeck, M. Reichstein, N. Carvalhais, and M. Heimann

Max Planck Institute for Biogeochemistry, Jena, Germany

Received: 14 June 2012 – Accepted: 9 October 2012 – Published: 29 October 2012

Correspondence to: B. Badawy (bbadawy@bgc-jena.mpg.de)

Published by Copernicus Publications on behalf of the European Geosciences Union.

Abstract

We present a Simple Diagnostic Photosynthesis and Respiration Model (SDPRM) that has been developed based on pre-existing formulations. The photosynthesis model is based on the light use efficiency logic, suggested by Monteith (1977), for calculating the Gross Primary Production (GPP) while the ecosystem respiration (R_{eco}) model is based on the formulations introduced by Lloyd and Taylor (1994) and modified by Reichstein et al. (2003). SDPRM is driven by satellite-derived fAPAR (fraction of Absorbed Photosynthetically Active Radiation) and climate data from NCEP/NCAR. The model estimates 3-hourly values of GPP for seven major biomes and daily R_{eco}. The motivation is to provide a-priori fields of surface CO_2 fluxes with fine temporal and spatial scales, and their derivatives with respect to adjustable model parameters, for atmospheric CO_2 inversions. The estimated fluxes from SDPRM showed that the model is capable of producing flux estimates consistent with the ones inferred from atmospheric CO_2 inversion or simulated from process-based models. In this Technical Note, different analyses were carried out to test the sensitivity of the estimated fluxes of GPP and R_{eco} to their driving forces. The spatial patterns of the climatic controls (temperature, precipitation, water) on the interannual variability of GPP are consistent with previous studies even though SDPRM has a very simple structure and few adjustable parameters, and hence it is much easier to modify than more sophisticated process-based models used in these previous studies. According to SDPRM, the results show that temperature is a limiting factor for the interannual variability of R_{eco} over the cold boreal forest, while precipitation is the main limiting factor of R_{eco} over the tropics and the southern hemisphere, consistent with previous regional studies.

BGD

9, 15127–15174, 2012

1 Introduction

The terrestrial biosphere plays an important role in the regional and the global carbon cycle, and thus the climate system. Nevertheless, the role of land ecosystems as sources or sinks of carbon in response to human perturbation is not well understood given the spatial heterogeneity and the temporal variability of the biospheric CO_2 exchange (Ciais et al., 2000). The terrestrial carbon cycle involves a set of biogeochemical processes that vary on a wide range of spatial and temporal scales. These processes can either reduce the level of atmospheric carbon or increase it, and are themselves sensitive to changes in climate, atmospheric CO_2, water availability, and land use. To understand the role of the terrestrial biosphere in the global carbon cycle, and thus their behavior in the future, it is crucial to quantify the processes that transfer carbon between the terrestrial biosphere and the atmosphere and their relations to the drivers.

Several techniques have been used to estimate carbon fluxes. Direct measurements of carbon fluxes using eddy covariance methods are an essential approach to measure and monitor carbon fluxes at local scales with high temporal resolution (Baldocchi, 2003). These measurements only represent the fluxes at the scale of the tower footprint, usually on the order of a few square kilometers or less (Baldocchi, 2003). There are many regions of the globe, the tropics in particular, where measurements are incomplete or entirely lacking. Thus, the coverage as well as the accuracy of these measurements is not sufficient for obtaining confidence at regional/global scales flux estimates (Friend et al., 2007).

On the other hand, atmospheric CO_2 measurements have played a key role in assessing source/sink distributions on global scales using atmospheric CO_2 inverse modeling (top-down approach) (e.g. Enting et al., 1995; Kaminski et al., 2002; Bousquet et al., 2000; Rödenbeck et al., 2003; Baker et al., 2006). However, consistent multi-year observations are currently only available at a discrete set of surface stations, which

BGD
9, 15127–15174, 2012

only provide large-scale information on surface fluxes. Moreover, the atmospheric concentration only reflects the combined effect of all processes acting at the surface.

Terrestrial biosphere models (bottom-up approaches) simulate the carbon fluxes between the atmosphere and the terrestrial system. These models range in complexity from simple regression "statistical" models to more complex process-based models. The simple statistical biosphere models are mainly based on empirical relations between one or more estimates of biological processes (e.g. soil respiration) and important climatic variables (e.g. temperature, precipitation) (e.g. Raich and Schlesinger, 1992; Lloyd and Taylor, 1994; Reichstein et al., 2003, 2005). On the other hand, the process-based models integrate knowledge of physiological and ecological processes to model the response of the system to environmental changes (Potter et al., 1993, 2012; McGuire et al., 2001; Sitch et al., 2008). Several studies have shown that the interannual variations (IAV) in ecosystem productivity simulated by different ecosystem models show large differences (McGuire et al., 2001; Schwalm et al., 2010; Keenan et al., 2012). This is because different models have different formulations representing ecosystem processes and environmental stresses that dominate the interannual variability. The validation of the terrestrial biosphere models is difficult on a large scale due to difficulties in scaling up small-scale measurements (e.g. eddy flux measurements)

Therefore, bottom-up terrestrial biosphere models and top-down inverse models have been combined into a multiple-constraint approach (e.g. Rayner et al., 2005). Key parameters of the biosphere model are optimized such that the mismatch between the modeled and the observed concentrations is minimized. This way, both the information on finer spatio-temporal resolution from the biosphere models and the large-scale atmospheric information is exploited. Optimizing model parameters instead of the fluxes themselves potentially also allows inferences about individual underlying processes.

Kaminski et al. (2002) introduced a systematic method for optimizing parameters. They optimized the controlling parameters of the Simple Diagnostic Biosphere Model (SDBM) introduced by Knorr and Heimann (1995) with respect to the seasonal cycle of atmospheric CO_2 concentrations. These optimized parameters are then used to run

BGD
9, 15127–15174, 2012

the model to predict some diagnostic quantities of interest such as net fluxes and Net Primary Productivity (NPP). A more complex approach, usually known as a Carbon Cycle Data Assimilation System (CCDAS), was introduced by Scholze et al. (2003) and Rayner et al. (2005). In CCDAS, they extended the work of Kaminski et al. (2002) by replacing SDBM by the more sophisticated prognostic terrestrial biosphere model, the Biosphere Energy Transfer Hydrology Scheme (BETHY) (Knorr, 2000). The model can run in prognostic mode to predict the behavior of the terrestrial biosphere under climate change. As the BETHY process model is not linear, the minimization algorithm in the CCDAS is a more involved process.

We envisage to apply this multiple-constraint approach using a biosphere model that is as simple as possible, but allows to use both seasonal and interannual signals in the atmospheric data. As a first step towards this, the aim of this Technical Note is to present the Simple Diagnostic Photosynthesis and Respiration Model (SDPRM) that we developed based on pre-existing formulations. Our goal is to provide a model that captures as much as possible fine-scale structure of the surface fluxes as provided in available driving fields, and involves a small set of parameters that can modify the model behavior on larger scales. By later coupling this model with the Jena inversion system, these adjustable parameters will be optimized based on atmospheric CO_2 data; this coupling will be described in a sub-sequent paper. Given this envisaged use of the model, we tried to set it up in a process-oriented way, but nevertheless essentially as an empirical relationship between Net Ecosystem Exchange and a set of driving variables expected to be the essential controls.

The outline of the Technical Note is as follows: Sect. 2 is devoted to the description of the empirical equations of the Simple Diagnostic Photosynthesis and Respiration Model (SDPRM) and the data used. Section 3 shows and discusses the results of the model. The global assessment of the importance of the climatic controls in limiting the interannual variability of GPP and R_{eco} are presented and discussed in Sect. 3.3.

BGD
9, 15127–15174, 2012

2 Simple Diagnostic Photosynthesis and Respiration Model (SDPRM)

Net Ecosystem Exchange of CO_2 (NEE) is the balance between the photosynthetic CO_2 uptake by plants through Gross Primary Production (GPP) and CO_2 emission through Ecosystem Respiration (R_{eco}), plant and soil respiration (NEE = R_{eco} – GPP). Many diurnal and seasonal patterns of atmospheric CO_2 concentration are dominated by only these two processes (Denning et al., 1996; Heimann et al., 1998). The Simple Diagnostic Photosynthesis and Respiration Model (SDPRM) expresses these two processes as an instantaneous function of the fraction of Absorbed Photosynthetically Active Radiation (fAPAR), and climate drivers (temperature, precipitation, and radiation). Additional processes including fire, dissolved organic carbon (DOC) and dissolved inorganic carbon (DIC) losses in rivers, erosion, and land use changes also influence the interannual and decadal dynamics in atmospheric CO_2 (Canadell et al., 2000; Pacala et al., 2001), but are not explicitly included into the model. SDPRM estimates 3-hourly values of GPP and daily R_{eco} over the period (1982–2006) on a grid-scale resolution (4° latitude × 5° longitude).

2.1 Data

2.1.1 GIMMS NDVI

SDPRM requires two types of satellite-based information: a land cover classification into plant functional types (PFTs), and fraction of Absorbed Photosynthetically Active Radiation (fAPAR) as a proxy for vegetation greenness. Previous studies show that changes in the Normalized Difference Vegetation Index (NDVI), the contrast between red and near-infrared reflectances of vegetation, indicate changes in vegetation conditions proportional to fAPAR (Sellers, 1985; Nemani and Running, 1989; Los et al., 2000). Therefore, the global NDVI dataset produced by the Global Inventory Modeling and Mapping Studies (GIMMS) – version g – was used to estimate fAPAR using an algorithm described by Los et al. (2000) (see Appendix A). The GIMMS NDVI data are

BGD
9, 15127–15174, 2012

available at the Global Land Cover Facility http://glcf.umiacs.umd.edu/ at a biweekly temporal resolution from 1982 to 2006 and a spatial resolution of 8 km × 8 km. The GIMMS NDVI data are derived from imagery obtained from the Advanced Very High Resolution Radiometer (AVHRR) instrument onboard the NOAA satellite series 7, 9, 11, 14, 16 and 17 (Tucker et al., 2005).

GIMMS NDVI data are chosen because they cover a much longer time period (1982–2006) compared to other satellite data sources (e.g. MODIS). The data are collected by a consistent series of instruments. In addition, several independent studies used earlier versions of the GIMMS NDVI data and showed reasonable agreement between GIMMS NDVI and other measures of vegetation (Davenport and Nicholson, 1993; Malmstrom et al., 1997; D'Arrigo et al., 2000). Nevertheless, as any satellite-based measurement, GIMMS NDVI suffers from numerous deficiencies including sensor degradation, cloud/snow contamination, limitation due to viewing geometry, and atmospheric effects. Therefore, GIMMS NDVI has been corrected by the data provider for some effects which are not related to vegetation change (Tucker et al., 2005). Nevertheless, it is still possible that after the corrections some contamination remains. Some sources of errors in the NDVI data set are not accounted for (i.e. soil background reflectance) as well. Therefore, GIMMS NDVI spatial/temporal variations for a certain region/time are affected by these corrections/errors, producing some variations, which may not related to actual variations in the vegetation. These errors in NDVI translate directly to errors in fAPAR.

2.1.2 Land cover classification

To produce a land cover classification into plant functional types (PFTs), the synergetic land cover dataset (SYNMAP) from Jung et al. (2006) are projected to the GIMMS NDVI grid (8 km × 8 km). Then, its classifications are aggregated into seven major PFTs (see Table 1 and Fig. 1). As a criterion of this aggregation, the spatial extent of the aggregated PFTs should not be too small in order to be distinguishable by the atmospheric observations through the later atmospheric inversion calculations. Therefore, classes

BGD
9, 15127–15174, 2012

of limited extent are joined to others of similar phenological properties. Also, all deciduous and mixed forests are joined into DxF (see Table 1) (despite ecological differences between them). The layout of the classes is a compromise between spatial diversity of these responses (demanding many classes) and the limited information available in the data (demanding few classes). For each PFT, a density map (fractional cover) $0 \leq \varrho_{\mathrm{PFT}}(x,y) \leq 1$ is obtained by summing up the density maps of the original land-surface classes:

$$\varrho_{\mathrm{PFT}}(x,y) = \sum_{\mathrm{class} \in \mathrm{PFT}} \varrho_{\mathrm{class}}(x,y). \quad (1)$$

The density map of all (non-ignored) land cover classes is written as:

$$\varrho_{\mathrm{veg}}(x,y) = \sum_{\mathrm{PFT}} \varrho_{\mathrm{PFT}}(x,y). \quad (2)$$

2.1.3 Meteorological data

SDPRM also needs meteorological fields (temperature, precipitation, short wave radiation, specific humidity) as input, taken from the improved reanalysis dataset from the National Center for Environmental Prediction/National Center for Atmospheric Research Reanalysis (NCEP/NCAR) (Kalnay et al., 1996) for the period 1982–2006. The NCEP/NCAR dataset consists of a reanalysis of the global observational network of meteorological variables (wind, temperature, pressure, humidity). Data are produced on a 2.5° × 2.5° grid box with temporal resolution of 6 h or daily. NCEP/NCAR dataset has been aggregated to the resolution of 4° latitude × 5° longitude as in SDPRM.

2.2 Photosynthesis model

GPP is commonly modeled as a function of climatic and soil variables, and uses satellite-derived estimates of the vegetation's light-absorbing properties (e.g. Randerson et al., 1996; Sellers et al., 1996b; Kaminski et al., 2002; van der Werf et al., 2004).

BGD
9, 15127–15174, 2012

In general, these models are known as light use efficiency (LUE) models, first introduced by (Monteith, 1977). Here, we follow MOD17, primary production products algorithm for calculating GPP (Running et al., 1999, 2004; Heinsch et al., 2003). The 3-hourly values of Gross Primary Production (GPP) is calculated as:

$$\mathrm{GPP} = \mathrm{PAR} \times \mathrm{fAPAR} \times \varepsilon \tag{3}$$

where ε ($\mathrm{gC\,MJ^{-1}}$) is the light use efficiency, fAPAR is the fraction of absorbed PAR, and PAR is calculated as 45 % of incident solar radiation I (Nobel, 1991) as:

$$\mathrm{PAR}(x,y,t) = 0.45 \cdot I(x,y,t) \tag{4}$$

The ε is calculated by attenuating maximum light use efficiency $\varepsilon_{\max}$ (mass of assimilated carbon per unit energy of absorbed radiation) via the effect of temperature (g_T) and vapor pressure deficit (g_{VPD}) factors as:

$$\varepsilon = \varepsilon_{\max} \cdot g_T \cdot g_{\mathrm{VPD}} \tag{5}$$

The attenuation factors g_T and g_{VPD} are simple ramp functions of daily minimum temperature $T_{\min}$ and vapor pressure deficit VPD. The dependence on daytime mean VPD is defined as:

$$g_{\mathrm{VPD}} = \begin{cases} 1, & \mathrm{VPD} < \mathrm{VPD}_1 \\ \frac{\mathrm{VPD}_0 - \mathrm{VPD}}{\mathrm{VPD}_0 - \mathrm{VPD}_1}, & \mathrm{VPD}_1 < \mathrm{VPD} < \mathrm{VPD}_0 \\ 0, & \mathrm{VPD} > \mathrm{VPD}_0 \end{cases} \tag{6}$$

The dependence on daily minimum temperature is defined as:

$$g_T = \begin{cases} 0, & T_{\min} < T_{\min,0} \\ \frac{T_{\min} - T_{\min,0}}{T_{\min,1} - T_{\min,0}}, & T_{\min,0} < T_{\min} < T_{\min,1} \\ 1, & T_{\min} > T_{\min,1} \end{cases} \tag{7}$$

BGD
9, 15127–15174, 2012

with $T_{min,0} = -8\,^{\circ}C$. The values of $T_{min,1}$, VPD_1 and VPD_0 are given in Table 2 for each PFT. Then, GPP formula for each PFT can be written as:

$$GPP_{PFT}(x,y,t) = \varepsilon_{max_{PFT}} \cdot \varrho_{PFT}(x,y) \cdot fPAR_{PFT}(x,y,t) \cdot PAR(x,y,t) \cdot g_{VPD_{PFT}}(x,y,t) \cdot g_{T_{PFT}}(x,y,t) \quad (8)$$

where $\varrho_{PFT}(x,y)$ is a density map (fractional cover) for each PFT (see Eq. 1). The values of $\varepsilon_{max_{PFT}}$ are given in Table 2 for each PFT. Incident radiation $I(x,y,t)$ is calculated from the downward shortwave radiation $I_{SW}(x,y,t)$ from NCEP meteorological reanalysis (Appendix B). Finally, $VPD(x,y,t)$ (difference between actual partial pressure of water vapor and saturation water vapor pressure, in Pa) is calculated as a daytime mean from specific humidity q ($kg\,kg^{-1}$), surface pressure $p \approx 101\,300$ Pa, air temperature at 2 m height T (°C), and the ratio $\kappa = 0.62197$ of the molar masses of water vs. air (Appendix C).

2.3 Ecosystem respiration model

The respiration model comprises both autotrophic and heterotrophic respiration because, due to similar dependencies on driving data, it is not expected that the signals from both can be separated from the atmospheric CO_2 measurements (in the later coupling the model to the inverse model). Following the formulations introduced by Lloyd and Taylor (1994) and Raich et al. (2002) and the modification made by Reichstein et al. (2003), the daily values of Ecosystem Respiration (R_{eco}) is calculated over all non-ignored land cover classes using the following equations:

$$R(x,y,t) = (R_0 + R_{LAI} \cdot r_{LAI}(x,y))\,\varrho_{veg}(x,y) \quad (9)$$

$$\cdot\, r_T[E, T(x,y,t)] \quad (10)$$

$$\cdot\, r_P[P_0, K, P(x,y,t)] \quad (11)$$

where R_0 (set to $0.8\,g\,C\,m^{-2}\,d^{-1}$) is the base respiration rate at the reference temperature, and R_{LAI} (set to $2.50\,g\,C\,m^{-2}\,d^{-1}$) is the respiration rate on maximum leaf area

BGD
9, 15127–15174, 2012

index, LAI_{max}). $\varrho_{veg}(x,y)$ is a density map of all non-ignored land cover classes (Eq. 2). The parameters R_0 and R_{LAI} are assumed constant over all PFTs because there is no solid information on how to break them down spatially. The leaf area index dependence ($r_{LAI}(x,y)$) is calculated as the average of the yearly maximum fAPAR value (Los et al., 2000) as:

$$r_{LAI}(x,y) = \overline{\max(\mathrm{fAPAR}(x,y,t))} \tag{12}$$

The temperature dependence is calculated as:

$$r_T[E,T] = \exp\left(-E\left[\frac{1}{T-T_0} - \frac{1}{T_{ref}-T_0}\right]\right) \tag{13}$$

where T (°C) is the daily temperature at 2 m obtained from NCEP/NCAR dataset, E = 135 K (the activation energy parameter of Lloyd and Taylor, 1994), T_0 = −46 °C (minimum temperature) as in Lloyd and Taylor (1994) and T_{ref} = 13 °C (reference temperature, taken from the 1901–2002 mean of the CRU dataset over land, available at University of East Anglia Climatic Research Unit (CRU) (http://www.cru.uea.ac.uk/). The precipitation dependence is written as:

$$r_P[P_0,K,P] = \frac{P+P_0}{P+P_0+K} \tag{14}$$

where P (mm month^{-1}) is the precipitation summed over the previous 30 days and K = 2.15 mm month^{-1} (the half-saturation constant of the hyperbolic relationship of soil respiration with monthly precipitation), taken from Reichstein et al. (2003). The parameter P_0 is fixed to the global value which is approximately 1.55 mm month^{-1} (95 % confidence interval: [0.2,2.5]) taken from Reichstein et al. (2003).

The a-priori values of the parameters (R_0, R_{LAI}, K, E) are modified from the soil-respiration values of Reichstein et al. (2003) assuming that soil respiration accounts for 60 % of ecosystem respiration. E corresponds to Q_{10} = 1.47 (Reichstein et al., 2003),

BGD
9, 15127–15174, 2012

which is a relatively low value, reflecting the fact that the present model is formulated in terms of air temperature (rather than the more usual soil temperature) which has more temporal variability than the temperature of the soil and most of the plant tissue that drive ecosystem respiration. The model introduced here has got the advantage over purely climate-driven models, since it accounts for important biological variation in soil respiration (Reichstein et al., 2003), while still being much simpler and easier to apply than process based models.

2.4 Filtering and aggregation

To test the performance of SDPRM, the estimated fluxes from the model are shown on a variety of spatial and temporal scales. The analysis mainly focus on the interannual variability and the monthly mean seasonal cycle of the flux estimates.

To obtain the interannual variability, the estimated fluxes are filtered by subtracting the mean seasonal cycle and most variations faster than 1 yr (filter with Gaussian spectral weights, as in Rödenbeck, 2005). This filter essentially retains annual averages. Likewise for the spatial resolution of the results, the estimated fluxes are integrated either into three latitudinal bands (90° S–20° S, 20° S–20° N and 20° N–90° N) or into the land regions as defined in the TransCom3 project (Gurney et al., 2002) (see Fig. 2).

3 Results and discussion

3.1 fAPAR

Figure 11 shows the time series of the full temporal variability and the running annual average (box-car filter) of the calculated fAPAR from GIMMS NDVI dataset. The time series is aggregated over three latitudinal bands (for a map of the regions see Fig. 2). In the Northern Hemisphere, fAPAR has striking seasonal changes, i.e. small values in winter and high values in summer, reflecting the vegetation phenology of the region. Over the tropics, the interannual variability has more variations because the major

BGD
9, 15127–15174, 2012

drivers associated with the growing season (e.g. precipitation, temperature) has high variations. Also, the natural variability in atmospheric aerosols and column water vapor may have created surface-independent variations in the GIMMS NDVI record (Tucker et al., 2005). As a consequence, fAPAR inherited these variations that may not be caused by vegetation variation. In June 1991, a major volcanic eruption occurred (the Pinatubo eruption), injecting large quantities of aerosols into the Earth's stratosphere. These aerosols and subsequent cooling can explain the decline in the interannual variability of fAPAR during the period from 1991–1993 over the tropics. Consequently, by using satellite-derived fAPAR dataset to drive the photosynthesis model, GPP estimates will be affected by a substantial variability in fAPAR that is not related to actual changes in vegetation function (see Sect. 3.2.1).

3.2 Model comparison

Kaminski and Heimann (2001) showed that using incorrect a-priori fluxes could seriously distort the inversion calculations. Therefore, we have performed several analysis to test the performance of the model and its ability to produce realistic a-priori fields for the inverse model. The estimates of NEE (R_{eco} – GPP) from SDPRM are compared with the land flux inferred from the atmospheric measurements of CO_2 using updated results from Rödenbeck (2005) (called here STD-inv). This is in order to asses to which extent the a-priori land fluxes from SDPRM are consistent in structure to the variability inferred from the atmospheric measurements.

Furthermore, the estimated carbon cycle components (GPP, R_{eco}) from SDPRM were compared with the results of the BIOME-BGCv1 process-based model (Trusilova and Churkina, 2008). BIOME-BGCv1 is based on the core of the BIOME-BGC version 4.1.1 (Thornton et al., 2005) point-based model. BIOME-BGC prognostically simulates the states and fluxes of carbon, nitrogen, and water within the vegetation, litter, and soil components of a terrestrial ecosystem (Appendix D). The BIOME-BGCv1 model uses the NCEP/NCAR meteorological fields as driving data.

BGD
9, 15127–15174, 2012

3.2.1 CfAPAR vs. VfAPAR

To explore the potential role of the contamination in the NDVI signal in fAPAR trends (a detailed analysis of this effect is beyond the scope of this Technical Note), we performed a sensitivity case assuming interannually constant vegetation by using the mean seasonal cycle of the fAPAR time series for the period 1982–2006 (hereafter referred to as SDPRM-CfAPAR). This is to remove the spurious variations in the fAPAR time series. Then the estimated NEE from SDPRM-CfAPAR is compared with NEE driven by the full temporal variability of the fAPAR time series (referred to as SDPRM-VfAPAR). In both runs, we used varying climate (daily NCEP/NCAR reanalysis data).

Figure 3 shows the comparison between the anomaly (deviation from the mean of 1982–2006) of the IAV of the calculated NEE from SDPRM-CfAPAR and SDPRM-VfAPAR and the estimated land flux from STD-inv. The fossil fuel emissions have been subtracted for STD-inv line. In the STD-inv, the yearly totals and geographical distribution of the fossil fuel emissions are taken from the Emission Database for Global Atmospheric Research (EDGAR) (Source: European Commission, Joint Research Centre (JRC)/Netherlands Environmental Assessment Agency (PBL). Emission Database for Global Atmospheric Research (EDGAR), release version 4.0. http://edgar.jrc.ec.europa.eu, 2009). In Fig. 3, we can see that the IAV of NEE from SDPRM-VfAPAR has some striking peaks, in particular over the tropics, during the period 1991–1993 compared to STD-inv. This can be explained by the variability in fAPAR (inherited from GIMMS NDVI) during the period from 1991–1993 over the tropical region due to the Pinatubo eruption, which injected large quantities of aerosols into the stratosphere. These aerosols, along with smoke from biomass burning and dust from soil erosion and other factors, can introduce significant variability in the AVHRR NDVI record (Tucker et al., 2005) and hence the fAPAR dataset. Also, the volcanic aerosols can reduce the photosynthetic activity by reducing the amount of sunlight reaching the vegetation (Oliveira et al., 2007; Krakauer and Randerson, 2003). The correlation analysis shows

BGD
9, 15127–15174, 2012

low correlation coefficient between the IAV of the global NEE time series from SDPRM-VfAPAR and the estimated global land flux from STD-inv (r = 0.31).

On the other hand, the IAV of NEE estimates from SDPRM-CfAPAR can capture a substantial fraction of the IAV of the land flux, despite the absence of interannual variations in fAPAR, as inferred from the atmospheric information using STD-inv. The correlation coefficient between the two land estimates is higher compared to the estimates from SDPRM-VfAPAR (r = 0.53). This suggests that most of the IAV of NEE is dominated by the climate signal (Mercado et al., 2009). This also indicates that the GIMMS NDVI data may be problematic in certain regions/periods and should be used with caution (Hall et al., 2006; Nemani et al., 2003).

Given that SDPRM do not include all the dynamics that are seen by the atmospheric CO_2 signals in STD-inv (fire, land use changes, etc.), we cannot expect to have a perfect match between SDPRM and STD-inv.

3.2.2 SDPRM vs. BIOME-BGCv1

The comparison between the calculated NEE from SDPRM-CfAPAR and NEE simulated by BIOME-BGCv1 is illustrated in Fig. 4 for 3 latitudinal bands (see Fig. 2). The land flux estimates from STD-inv is shown in the same figure. It shows that the IAV of NEE from SDPRM-CfAPAR (Fig. 4b) has a similar pattern compared to the NEE simulated by the BIOME-BGCv1 model, in particular over the tropics (r = 0.63). Similarly, Fig. 5b shows the same comparison but for TransCom3 land regions (see Fig. 2). SDPRM-CfAPAR and BIOME-BGCv1 agree in many temporal features over most of the regions. In contrast, STD-inv has higher IAV of the land flux as well as a different pattern compared to SDPRM-CfAPAR and BIOME-BGCv1. Due to the scarcity of the atmospheric CO_2 observations, the results of STD-inv might not be well constrained over smaller regions. Also, missing processes (e.g. fire) in the biosphere models can also be the reason for the discrepancies between the flux variability shown in Fig. 5b.

The monthly mean seasonal cycle of the flux estimates from the three models are shown in Fig. 4a and Fig. 5a. The general phase of the seasonal cycle of NEE

BGD
9, 15127–15174, 2012

from SDPRM-CfAPAR is similar to the seasonal cycle of the land flux estimated from STD-inv over Northern Hemisphere land (NH), though the amplitude is higher in SDPRM-CfAPAR. In terms of phasing, however, SDPRM-CfAPAR agrees much better to the atmospheric information (STD-inv) compared to the more sophisticated model (BIOME-BGCv1), which leads STD-inv by about 2 months in various regions, especially in the northern high-latitudes.

In addition to NEE, we also compare the carbon cycle components (GPP and R_{eco}) from SDPRM-CfAPAR with the results from BIOME-BGCv1, for both the monthly mean seasonal cycle and IAV (Fig. 6 and Fig. 7). The comparisons show that GPP and R_{eco} from SDPRM-CfAPAR agree well with those from BIOME-BGCv1 although both models are using different algorithms for calculating GPP and R_{eco}. In the MOD17 algorithm used in SDPRM, VPD is the only variable directly related to environmental water stress, while both VPD and soil water content are used for water stress calculations in BIOME-BGCv1.

In Fig. 7a, the monthly mean seasonal cycles of R_{eco} from SDPRM and BIOME-BGCv1 are presented. As mentioned earlier, the parameters and the structure of the respiration model in SDPRM were chosen from the soil-respiration model of Reichstein et al. (2003) which was calibrated using field measurements from Europe and North America. Also, R_{eco} is calculated in SDPRM using only climate drivers and maximum fAPAR and independent of GPP. But in real world R_{eco} is strongly connected to GPP on seasonal timescales (Mahecha et al., 2010; Migliavacca et al., 2011). This might explain why SDPRM is underestimating the amplitude of the seasonal cycle of R_{eco} compared to BIOME-BGCv1, in particular over Europe, North American Temperate and Boreal and Eurasian Boreal (see Fig. 7a).

3.2.3 Summary

Though a comprehensive evaluation of SDPRM against independent data sources is a significant challenge (e.g. due to the contrast between the point-scale nature of the ground-based flux measurements on the order of a few square kilometers or

BGD
9, 15127–15174, 2012

less Baldocchi, 2003) and the spatial resolution of SDPRM (4° latitude × 5° longitude), we conclude from the comparison between SDPRM-CfAPAR, BIOME-BGCv1 and the STDinv, that SDPRM-CfAPAR –despite its simple structure – is capable of reproducing flux patterns compatible to the ones inferred from the atmospheric measurements or inferred based on process understanding. This is important in light of its intended use.

3.3 Climate limitations

Understanding responses of GPP and R_{eco} to climate controls is crucial to understand terrestrial carbon cycle and climate feedbacks in the future. Many studies have shown strong relationships between the annual climate (means) and ecosystem productivity (e.g. Stephenson, 1990; Churkina and Running, 1998; Valentini et al., 2000; Nemani et al., 2003; Running et al., 2004; Wang et al., 2011, and others). They also show that any small variation in the annual climate can have a significant impact on the plant growth and biome stability. Thus, it seems reasonable to use the year-to-year variation (interannual variability (IAV)) of climate variables as indicators of the ecosystem productivity limitation. Here, we performed an analysis to assess the importance of the climatic controls in limiting GPP and R_{eco}. This is done by evaluating the contribution of each climate variable (used to drive SDPRM) to the interannual variations of GPP and R_{eco}.

We tested the effects of interannual variation in each climate variable by removing the IAV of the other climate variables (using only the mean seasonal cycle for the period 1982 to 2006, applied repeatedly every year) and using constant vegetation (mean seasonal cycle fAPAR as in run SDPRM-CfAPAR). In the case of GPP, simulations allow for the isolation of the effects of daily minimum temperature (GT: minimum temperature only varying and other climate drivers constant (mean seasonal cycle)), vapor pressure deficit (GV: VPD only varying and other climate drivers constant), and downward short wave radiation (GS: radiation only varying and other climate drivers constant). In the case of R_{eco}, simulations allow isolation of the effects daily temperature (RT: daily temperature only varying and other climate drivers constant), and precipitation (RP:

BGD
9, 15127–15174, 2012

precipitation only varying and other climate drivers constant). Then, the relative contribution of each independent climate variable on GPP and R_{eco} estimates (1982–2006) is calculated with a logic similar to the one suggested by Ichii et al. (2005) which can be expressed as:

$$GC_i = \frac{\sigma^2_{G_i}}{\sigma^2_{GT} + \sigma^2_{GV} + \sigma^2_{GS}} \quad (15)$$

$$RC_i = \frac{\sigma^2_{R_i}}{\sigma^2_{RT} + \sigma^2_{RP}} \quad (16)$$

where GC_i and RC_i are the proportional contribution of $\sigma^2_{G_i}$ and $\sigma^2_{R_i}$, the variance of the anomalies of the interannual variability of GPP and R_{eco}, respectively, for each of the sensitivity cases (G_i = GT, GV, or GS, while R_i = RT or TP), to the sum of the variance of all of the sensitivity cases. High/low GC_i or RC_i indicates large/small contribution of the climate driver i on overall variance.

Based on the calculations of the squared correlation coefficient (R^2), we found that GPP anomalies in the default run (SDPRM-CfAPAR – constant vegetation and all climate variables are varying) were mostly explained by the sum of all sensitivity runs (one variable is varying and the others are constants) (R^2 = 0.98). The same is found for R_{eco}. This indicates that the main effects were essentially additive and that extensive non-linear interactions do not exist. Therefore, non-linear responses of GPP or R_{eco} to interactions among climate variables (e.g. simultaneous changes in temperature and radiation) were not investigated.

3.3.1 Climate controls on GPP

Based on Eq. (15), Fig. 8 shows the global distribution of the relative contribution of each climate variable (temperature, vapor pressure deficit, and radiation) to the IAV of

BGD
9, 15127–15174, 2012

GPP. The results are also summarized in Table 3 for different eco-regions. The following features can be observed:

Temperature: in the high latitudes, temperature is clearly the primary control on GPP (Fig. 8a), in particular over the North American boreal forest and Eurasian boreal forest (77 % and 63 %, respectively) and to a lesser extent over Europe and the Eurasian temperate forest (27 % and 13 %, respectively, see Table 3). On average, temperature limits GPP over the Northern Hemisphere by almost 43 %. This can be explained by the fact that at low temperatures the enzymes responsible for photosynthesis are inhibited. Thus, very low mean annual temperatures limit plant productivity as in the case of tundra and boreal forests in northern latitudes. On the other hand, the tropics and the Southern Hemisphere areas are not limited by low temperature (less than 2 %). Similar findings were presented by Nemani et al. (2003), who investigated vegetation responses to climatic changes by analyzing 18 yr (1982 to 1999) of both climatic data and satellite observations of vegetation activity. According to their study, cold winter temperatures limit high-latitude Eurasian vegetation, while tropical areas are never limited by low temperatures.

Vapor pressure deficit: as mentioned earlier, in the MOD17 algorithm for calculating GPP, VPD is the only variable directly related to environmental water stress. Therefore, VPD is used as an indicator of environment water stress. It is clear from Fig. 8b that VPD is a dominant control on GPP over large areas of the globe where water is severely limited, mainly Australia (91 %), North and South American temperate forest (77 % and 76 %, respectively), Southern Africa (76 %), Southern Europe (56 %), and the Sahara desert (58 %) (see Table 3). This is also consistent with the finding of Nemani et al. (2003) who estimated that water availability most strongly limits vegetation growth over 40 % of the Earth's vegetated surface, and vapor pressure deficit (VPD) is a limiting factor of vegetation growth in water-limited ecosystems of Australia, Africa, and the Indian subcontinent.

Radiation: radiation is another important limiting factor on GPP, as it represents the energy source of photosynthesist. Interannual variations in radiation result from

BGD
9, 15127–15174, 2012

interannual variations in cloud cover. According to that, we can see in Fig. 8c that radiation limits GPP by almost 56 % over the area covered most of the year by cloud (tropical regions). But radiation is also a limiting control on GPP, over some areas in the Northern Hemisphere, such as Eurasian temperate (39 %), Europe (17 %), and North American temperate (14 %), though to a lesser degree. Nemani et al. (2003) also found that radiation is a limiting factor in Western Europe and the equatorial tropics regions.

3.3.2 Climate controls on R_{eco}

Similarly, based on Eq. (16), Fig. 9 shows the global distribution of the relative contribution of each climate variable (temperature, precipitation) to the interannual variability of R_{eco}. Additionally, the calculated values based on Eq. (16) for different regions are shown in Table 3. The results of the relative contribution of each climate factor to R_{eco} are summarized as follows:

Temperature: similar to GPP, temperature partially determines the respiration rates of vegetation. Consequently, plants growing in cold regions are usually less productive. Thus, R_{eco} of plants from cold regions is primarily limited by temperature. Figure 9 shows that clearly, where temperature limits R_{eco} by almost 87 % over the Northern Hemisphere and by a lower rate over tropical regions (49 %). The results consistent with the regional studies in particular over the boreal ecosystems (e.g. Wang et al., 2011).

Precipitation: Fig. 9 shows that precipitation is a dominant control on R_{eco} over large areas of the globe where water is severely limiting, in particular the tropics and Southern Hemisphere regions (51 % and 83 %, respectively).

4 Discussion and conclusions

In this Technical Note, we presented and evaluated the Simple Diagnostic Photosynthesis and Respiration Model (SDPRM). The model estimates 3-hourly values of Gross

BGD
9, 15127–15174, 2012

Primary Production (GPP) and daily values of ecosystem respiration (R_{eco}). The spatial resolution of the model is 4° latitude × 5° longitude. The model is driven by climate data from NCEP/NCAR and satellite-derived fAPAR data.

Given the coarse spatial resolution of SDPRM, ground-based flux measurements cannot be used to validate the results directly. Therefore, to test the performance of the model, we compared the carbon flux components (NEE, GPP, and R_{eco}) with two different approaches for estimating the land fluxes, (1) the process-understanding approach presented by the BIOME-BGCv1 model, and (2) the atmospheric CO_2 inversion in which the land fluxes are inferred from the atmospheric information. It is found that, by using climatological fAPAR and varying climate data, SDPRM-CfAPAR is capable of reproducing flux patterns comparable to the ones inferred from the atmospheric measurements or simulated based on process understanding. This indicates that, in the SDPRM, interannual variability (IAV) of NEE, to some extent, is mainly driven by climate (despite the missing processes, e.g. fire) and not by vegetation changes. Furthermore, we have tested the sensitivities of GPP and R_{eco} to the driving climate variables, by estimating the relative contribution of individual climate variables to the interannual variability of GPP and R_{eco}. Based on the analysis, low temperature controls the IAV of GPP mainly over high-latitude Eurasian vegetation. Over the tropics, radiation is the main limiting factor of the IAV of GPP. VPD controls the IAV of GPP in water-limited ecosystems. Temperature controls the IAV of R_{eco} over large areas of the globe, in particular over Northern Hemisphere regions. Also, precipitation controls the IAV of R_{eco} over large areas of the globe, in particular over the tropics and Southern Hemisphere regions.

SDPRM has the advantage that it uses few driving variables and few adjustable parameters, and thus is flexible to be optimized in an inversion. However, the simplification of our model structure can lead to considerable uncertainty in regional flux estimates. For example, the model uses constant parameters that specified globally or for only 7 PFTs. But in real world, these parameters are controlled by details of species composition, site history including changes in land use, etc., and thus can result in substantial

BGD
9, 15127–15174, 2012

variability in regional flux estimates. Also, deficiencies in the spatial resolution and the accuracy of land cover representation can lead to considerable uncertainty in the flux estimates. The current classification may have to be revised based on future diagnostics. However, the present choice does not seem a-priori unreasonable to us, because the aggregation of pixels into the same class only means that the response of the local flux to the local climate is forced to be the same. As mentioned earlier, the dependency on GPP might need to be included as an additional driver of R_{eco} (Mahecha et al., 2010; Migliavacca et al., 2011). The biases in NCEP/NCAR reanalyses also can introduce substantial error into GPP and R_{eco} estimates. The other limitation of SDPRM is the missing of important processes (e.g. fire emissions).

The model will replace, in a subsequent paper, the simple statistical flux representation of the inversion algorithm presented by Rödenbeck (2005) to optimize key parameters of the model in order to fit the observed CO_2 concentrations. Optimizing model parameters instead of the fluxes themselves can provide flux estimates that are structurally consistent with the process parameterizations used. Different parameter configurations can be tested to determine which parameters are globally valid and which have to be spatially explicit. Due to the missing processes in SDPRM, we expect that the model will not be able to fit the observed concentration completely; however, the residual fluxes corresponding to the residual between the modeled and the observed concentration can then be used to investigate the contribution of some of the missing processes, as will be discussed in more details in the sub-sequent paper.

Appendix A

fAPAR

fAPAR is calculated following the approach described in Goward and Huemmrich (1992) and Sellers et al. (1996a) and further adapted by Los et al. (2000). Two linear equations between fAPAR and NDVI are described, referred to as the $fAPAR_{NDVI}$

BGD
9, 15127–15174, 2012

and $fAPAR_{SR}$ models. In the $fAPAR_{NDVI}$ model, maximum and minimum NDVI values for each vegetation type are related to maximum and minimum fAPAR according to:

$$fAPAR_{NDVI} = \frac{(NDVI - NDVI_{min})(fAPAR_{range})}{NDVI_{range}} + fAPAR_{min} \quad (A1)$$

where $NDVI_{range} = NDVI_{max} - NDVI_{min}$ corresponds to the difference between the 98th and 2nd percentiles of the NDVI frequency distribution estimated per PFT (see Table 4). The parameter $fAPAR_{range}$ equals $fAPAR_{max} - fAPAR_{min} = 0.95 - 0.01$. In the $fAPAR_{SR}$ model, fAPAR is linearly related to the simple ratio (SR) which can be expressed as a transformation of NDVI:

$$SR = \frac{1 + NDVI}{1 - NDVI} \quad (A2)$$

$$fAPAR_{SR} = \frac{(SR - SR_{min})(fAPAR_{range})}{SR\_range} + fAPAR_{min} \quad (A3)$$

where $SR_{range} = SR_{max} - SR_{min}$ corresponds to the difference between the 98th and 2nd percentiles of the SR frequency distribution. Based on the study of Los et al. (2000), in $fAPAR_{NDVI}$ relationships, NDVI values was not corrected for the effect of the atmosphere (i.e. water vapor and aerosols) that causes significant overestimates of fAPAR. In $fAPAR_{SR}$ relationships, atmospheric effects are partially accounted for by the statistical selection of NDVI values, but still it produces significant underestimates of fAPAR. According to Los et al. (2000), an intermediate model, calculating the average fAPAR of the $fAPAR_{NDVI}$ and $fAPAR_{SR}$ models, performed better by giving the smallest bias in fAPAR estimates in comparison to the ground-measured fAPAR. Accordingly, fAPAR is calculated using the following relationship:

$$fAPAR = \frac{fAPAR_{SR} + fAPAR_{NDVI}}{2} \quad (A4)$$

BGD
9, 15127–15174, 2012

These calculations are done on a pixel basis with 8 km × 8 km spatial resolution. After that, the fAPAR data have been aggregated to a spatial resolution of 4° latitude × 5° longitude. Then, a separate dataset, $fAPAR_{PFT}$, is created for each PFT.

Appendix B

Incident radiation

Incident radiation $I(x,y,t)$ is calculated from the downward shortwave radiation $I_{SW}(x,y,t)$ from NCEP meteorological reanalysis, which contains both the seasonal and synoptic variability, while the diurnal variation is only coarsely represented in the 6-hourly fields. Therefore, incident radiation is calculated as:

$$I(x,y,t) = j(x,y,t) \cdot I_0(x,y,t) \quad \text{(B1)}$$

where $I_0(x,y,t)$, from the purely geometrical clear-sky radiation, is:

$$I_0(x,y,t) = \max(0, \sin(y) \cdot \sin(x_\Delta) + \cos(y) \cdot \cos(x_\Delta) \cdot \cos(x_h)) \quad \text{(B2)}$$

with

$$x_h = 360° r_{day}(t) + x - 180° \quad \text{(B3)}$$

$$x_\Delta = -23.4° \cdot \cos(360° r_{year}(t) + 10°) \quad \text{(B4)}$$

where $r_{day}(t)$ and $r_{year}(t)$ give the fractions of the day (since 00Z UTC) and of the year (since 1 January) at time t, and x and y are taken to represent longitude and latitude. The cloud factor $j(x,y,t)$ is obtained by the following equation at the 6-hourly meteorological intervals, and linearly interpolated in between.

$$j(x,y,t) = \frac{I_{SW}(x,y,t)}{I_0(x,y,t)} \quad \text{(B5)}$$

BGD
9, 15127–15174, 2012

Appendix C

Vapor Pressure deficit (VPD)

VPD(x, y, t) (difference between actual partial pressure of water vapor and saturation water vapor pressure in Pa) is calculated as a daytime mean from specific humidity q ($\mathrm{kg\,kg^{-1}}$), sea level pressure p (Pa) $\approx 101\,300$ Pa, air temperature at 2 m height T (°C), and the ratio $\kappa = 0.62197$ of the molar masses of water vs. air as:

$$\mathrm{VPD} = 611 \cdot \exp\left(\frac{17.26938818 \cdot T}{237.3 + T}\right) - \frac{q \cdot p}{\kappa - q(\kappa - 1)} \tag{C1}$$

The daytime average was done using $I_0(x, y, t)$ from Eq. (B2) as weighting, and applying a triangular filter to de-diurnalize.

Appendix D

BIOME-BGCv1

In BIOME-BGCv1, the total ecosystem respiration (R_{eco}) includes three components: maintenance respiration (MR), growth respiration (GR), and heterotrophic respiration (HR). MR of each plant compartment is computed as a function of compartment nitrogen content and temperature. GR is calculated on the basis of construction costs by plant compartment. Different construction costs are applied to woody and non-woody plant tissues. HR includes decomposition of both litter and soil. It is related to their chemical composition (cellulose, lignin, and humus), to their carbon to nitrogen ratios, to soil mineral nitrogen availability and to soil moisture and temperature. The Gross Photosynthetic Production (GPP) is calculated based on absorbed photosynthetically active radiation, atmospheric carbon dioxide concentration, air temperature, vapor pressure deficit, soil water content, atmospheric nitrogen deposition, the leaf

BGD
9, 15127–15174, 2012

area index, and available nitrogen content in soil. For the comparison, the BIOME-BGCv1 results were aggregated from 0.5° × 0.5° to the spatial resolution of 4° × 5° as in SDPRM and STD-inv. Further details about the structure of BIOME-BGCv1 are described in Trusilova et al. (2009).

Acknowledgements. The authors would like to thank the Max Planck Society for providing funding and facilities, Martin Jung for providing us with SYNMAP data, Miguel D. Mahecha for fruitful discussions about statistical analyses, Sönke Zaehle for his helpful comments. We would also like to thank Global Land Cover Facility, University of Maryland for making NDVI GIMMS data available for free.

The service charges for this open access publication have been covered by the Max Planck Society.

References

Baker, D. F., Doney, S. C., and Schimel, D. S.: Variational data assimilation for atmospheric CO_2, Tellus B, 58, 359–365, 2006. 15129

Baldocchi, D. D.: Assessing ecosystem carbon balance: problems and prospects of the eddy covariance technique, Global Change Biol., 9, 479–492, 2003. 15129, 15142

Bousquet, P., Peylin, P., Ciais, P., Le Quéré, C., Friedlingstein, P., and Tans, P. P.: Regional changes in carbon dioxide fluxes of land and oceans since 1980, Science, 290, 1342–1346, 2000. 15129

Canadell, J. G., Mooney, H. A., Baldocchi, D. D., Berry, J. A., Ehleringer, J. R., Field, C. B., Gower, S. T., Hollinger, D. Y., Hunt, J. E., Jackson, R. B., Running, S. W., Shaver, G. R., Steffen, W., Trumbore, S. E., Valentini, R., and Bond, B. Y.: Carbon Metabolism of the Terrestrial Biosphere: A Multitechnique Approach for Improved Understanding, Ecosystems, 3, 115–130, 2000. 15132

Churkina, G. and Running, S.: Contrasting climatic controls on the estimated productivity of global terrestrial biomes, Ecosystems, 1, 206–215, 1998. 15143

Ciais, P., Peylin, P., and Bousquet, P.: Regional Biospheric Carbon Fluxes as Inferred from Atmospheric CO_2 Measurements, Ecol. Appl., 10, 1574–1589, 2000. 15129

BGD

9, 15127–15174, 2012

D'Arrigo, R. D., Malmstrom, C. M., Jacoby, G. C., Los, S. O., and Bunker, D. E.: Correlation between maximum latewood density of annual tree rings and NDVI based estimates of forest productivity, Int. J. Remote Sens., 21, 2329–2336, 2000. 15133

Davenport, M. L. and Nicholson, S. E.: On the Relation between Rainfall and the Normalized Difference Vegetation Index for Diverse Vegetation Types in East Africa, Int. J. Remote Sens., 14, 2369–2389, doi:10.1080/01431169308954042, 1993. 15133

Denning, A. S., Collatz, G. J., Zhang, C. G., Randall, D. A., Berry, J. A., Sellers, P. J., Colello, G. D., and Dazlich, D. A.: Simulations of terrestrial carbon metabolism and atmospheric CO_2 in a general circulation model. 1. Surface carbon fluxes, Tellus B, 48, 521–542, 1996. 15132

Enting, I., Trudinger, C. M., and Francey, R. J.: A synthesis inversion of the concentration and $\delta^{13}C$ of atmospheric CO_2, Tellus, 47B, 35–52, 1995. 15129

Friend, A. D., Arneth, A., Kiang, N. Y., Lomas, M., Ogée, J., Rödenbeckk, C., Running, S. W., Santaren, J.-D., Sitch, S., Viovy, N., Woodward, F. I., and Zaehle, S.: FLUXNET and modelling the global carbon cycle, Global Change Biol., 13, 610–633, 2007. 15129

Goward, S. N. and Huemmrich, K. F.: Vegetation canopy PAR absorbtance and the normalized difference vegetation index: An assessment using the SAIL model, Remote Sens. Environ., 39, 119–140, 1992. 15148

Gurney, K. R., Law, R. M., Denning, A. S., Rayner, P. J., Baker, D., Bousquet, P., Bruhwiler, L., Chen, Y.-H., Ciais, P., Fan, S., Fung, I. Y., Gloor, M., Heimann, M., Higuchi, K., John, J., Maki, T., Maksyutov, S., Masarie, K., Peylin, P., Prather, M., Pak, B. C., Randerson, J., Sarmiento, J., Taguchi, S., Takahashi, T., and Yuen, C.-W.: Towards robust regional estimates of CO_2 sources and sinks using atmospheric transport models, Nature, 415, 626–630, 2002. 15138, 15165

Hall, F., Masek, J. G., and Collatz, G. J.: Evaluation of ISLSCP Initiative II FASIR and GIMMS NDVI products and implications for carbon cycle science, J. Geophys. Res., 111, 15 pp. doi:10.1029/2006JD007438, 2006. 15141

Heimann, M., Esser, G., Haxeltine, A., Kaduk, J., Kicklighter, D. W., Knorr, W., Kohlmaier, G. H., McGuire, A. D., Melillo, J., Moore III, B., Otto, R. D., Prentice, I. C., Sauf, W., Schloss, A., Sitch, S., Wittenberg, U., and Würth, G.: Evaluation of terrestrial carbon cycle models through simulations of the seasonal cycle of atmospheric CO_2: First results of a model intercomparison study, Glob. Biogeochem. Cy., 12, 1–24, 1998. 15132

Heinsch, F. A., Reeves, M., Votava, P., Kang, S. Y., Milesi, C., Zhao, M. S., Glassy, J., Jolly, W. M., Loehman, R., Bowker, C. F., Kimball, J. S., Nemani, R. R., and Running, S. W.: User's

BGD
9, 15127–15174, 2012

Guide, GPP and NPP (MOD 17A2/A3) Products, NASA MODIS Land Algorithm [Online], available at: http://www.ntsg.umt.edu/modis/MOD17UsersGuide.pdf, last access: 31 December 2009, 2003. 15135

Ichii, K., Hashimoto, H., Nemani, R., and White, M.: Modeling the interannual variability and trends in gross and net primary productivity of tropical forests from 1982 to 1999, Global Planet. Change, 48, 274–286, 2005. 15144

Jung, M., Henkel, K., Herold, M., and Churkina, G.: Exploiting synergies of global land cover products for carbon cycle modeling, Remote Sens. Environ., 101, 534–553, 2006. 15133, 15160, 15164

Kalnay, E., Kanamitsu, M., Kistler, R., Collins, W., Deaven, D., Gandin, L., Iredell, M., Saha, S., White, G., Woollen, J., Zhu, Y., Chelliah, M., Ebisuzaki, W., Higgins, W., Janowiak, J., Mo, K. C., Ropelewski, C., Wang, J., Leetmaa, A., Reynolds, R., Jenne, R., and Joseph, D.: The NCEP/NCAR 40-year reanalysis project, Bull. Am. Met. Soc., 77, 437–471, 1996. 15134

Kaminski, T. and Heimann, M.: Inverse modeling of atmospheric carbon dioxide fluxes, Science, 294, p. 259, doi:10.1126/science.294.5541.259a, 2001. 15139

Kaminski, T., Knorr, W., Rayner, P. J., and Heimann, M.: Assimilating atmospheric data into a terrestrial biosphere model: A case study of the seasonal cycle, Glob. Biogeochem. Cy., 16, 1066, doi:10.1029/2001GB001463, 2002. 15129, 15130, 15131, 15134

Keenan, T. F., Baker, I., Barr, A., Ciais, P., Davis, K., Dietze, M., Dragoni,D., Gough, C. M., Grant, R., Hollinger, D., Hufkens, K., Poulter, B., McCaughey, H., Raczka, B., Ryu, Y., Schaefer, K., Tian, H., Verbeeck, H., Zhao, M., and Richardson, A.: Terrestrial biosphere model performance for inter-annual variability of land-atmosphere CO_2 exchange, Global Change Biol., 18, 1971–1987 doi:10.1111/j.1365-2486.2012.02678.x, 2012. 15130

Knorr, W.: Annual and interannual CO_2 exchanges of the terrestrial biosphere: process based simulations and uncertainties, Global Ecol. Biogeogr., 9, 225–252, 2000. 15131

Knorr, W. and Heimann, M.: Impact of drought stress and other factors on seasonal land biosphere CO_2 exchange studied through an atmospheric tracer transport model, Tellus B, 47, doi:10.1034/j.1600-0889.47.issue4.7.x, 1995. 15130

Krakauer, N. Y. and Randerson, J. T.: Do volcanic eruptions enhance or diminish net primary production? Evidence from tree rings, Glob. Biogeochem. Cy., 17, 1118, doi:10.1029/2003GB002076, 2003. 15140

Lloyd, J. and Taylor, J. A.: On the temperature dependence of soil respiration, Funct. Ecol., 8, 315–323, 1994. 15128, 15130, 15136, 15137

BGD
9, 15127–15174, 2012

Los, S. O., Pollack, N. H., Parris, M. T., Collatz, G. J., Tucker, C. J., Sellers, P. J., Malmström, C. M., DeFries, R. S., Bounoua, L., and Dazlich, D. A.: A Global 9-yr Biophysical Land Surface Dataset from NOAA AVHRR Data, J. Hydrometeorol., 1, 183–199, 2000. 15132, 15137, 15148, 15149

Mahecha, M. D., Reichstein, M., Carvalhais, N., lasslop, G., Lange, H., Seneviratne, S. I., Vargas, R., Ammann, C., Arain, M. A., Cescatti, A., Janssens, I. A., Migliavacca, M., Montagnani, L., and Richardson, A.: Global Convergence in the Temperature Sensitivity of Respiration at Ecosystem Level, Science, 329, 838–840, doi:10.1126/science.1189587, 2010. 15142, 15148

Malmstrom, C. M., Thompson, M. V., Juday, G. P., Los, S. O., Randerson, J. T., and Field, C. B.: Interannual variation in global-scale net primary production: Testing model estimates, Glob. Biogeochem. Cy., 33, 481–486, 1997. 15133

McGuire, A. D., Sitch, S., Clein, J. S., Dargaville, R., Esser, G., Foley, J., Heimann, M., Joos, F., Kaplan, J., Kicklighter, D. W., Meier, R. A., Melillo, J. M., Moore III, B., Prentice, I. C., Ramankutty, N., Reichenau, T., Schloss, A., Tian, H., Williams, L. J., and Wittenberg, U.: Carbon balance of the terrestrial biosphere in the twentieth century: Analyses of CO_2, climate and land use effects with four process-based ecosystem models, Glob. Biogeochem. Cy., 15, 183–206, 2001. 15130

Mercado, L., Bellouin, N., Sitch, S., Boucher, O., Huntingford, C., Wild, M., and Cox, P. M.: Impact of changes in diffuse radiation on the global land carbon sink, Nature, 458, 1014–1017, doi:10.1038/nature07949, 2009. 15141

Migliavacca, M., Reichstein, M., Richardson, A. D., Colombo, R., Sutton, M. A., lasslop, G., Tomelleri, E., Wohlfahrt, G., Carvalhais, N., Cescatti, A., Mahecha, M. D. D., Montagnani, L., Papale, D., Zaehle, S., ARAIN, A., Arneth, A., Black, T. A., Carrara, A., Dore, S., Gianelle, D., helfter, C., Hollinger, D., Kutsch, W. L., Lafleur, P. M., Nouvellon, Y., Rebmann, C., da Rocha, H. R., Rodeghiero, M., Roupsard, O., SEBASTIÀ, M. T., Seufert, G., Soussana, J. F., and van der Molen, M. K. K.: Semiempirical modeling of abiotic and biotic factors controlling ecosystem respiration across eddy covariance sites, Global Change Biol., 17, 390–409, 2011. 15142, 15148

Monteith, J. L.: Climate and efficiency of crop production in Britain, Philos. T. Roy. Soc. B, 281, 277–294, 1977. 15128, 15135

BGD
9, 15127–15174, 2012

Nemani, R. R. and Running, S. W.: Estimation of Regional Surface Resistance to Evapotranspiration from NDVI and Thermal-IR AVHRR Data, J. Appl. Meteorol., 28, 276–284, 1989. 15132

Nemani, R. R., Keeling, C. D., Hashimoto, H., Jolly, W. M., Piper, S. C., Tucker, C. J., Myneni, R. B., and Running, S. W.: Climate-driven increases in global terrestrial net primary production from 1982 to 1999, Science, 300, 1560–1563, 2003. 15141, 15143, 15145, 15146

Nobel, P. S.: Phsiochemical and Environmental Plant Physiology, Academic Press, San Diego, California, 1991. 15135

Oliveira, P. H. F., Artaxo, P., Pires, C., lucca, S. D., Procopio, A., Holben, B., Schafer, J., Cardoso, L. F., Wofsy, S. C., and Rocha, H. R.: The effects of biomass burning aerosols and clouds on the CO_2 flux in Amazonia, Tellus B, 59, 338–349, 2007. 15140

Pacala, S. W., Hurtt, G. C., Baker, D., Peylin, P., Houghton, R. A., Birdsey, R. A., Heath, L., Sundquist, E. T., Stallard, R. F., Ciais, P., Moorcroft, P., Caspersen, J. P., Shevliakova, E., Moore, B., Kohlmaier, G., Holland, E., Gloor, M., Harmon, M. E., Fan, S.-M., Sarmiento, J. L., Goodale, C. L., Schimel, D., and Field, C. B.: Consistent land- and atmosphere-based US carbon sink estimates, Science, 292, 2316–2320, 2001. 15132

Potter, C., Klooster, S., Genovese, V., Hiatt, C., Boriah, S., Kumar, V., Mithal, V., and Garg, A.: Terrestrial Ecosystem Carbon Fluxes Predicted from MODIS Satellite Data and Large-Scale Disturbance Modeling, Int. J. Geosci., 3, 469–479, 2012. 15130

Potter, C. S., Randerson, J. T., Field, C. B., Matson, P. A., Vitousek, P. M., Mooney, H. A., and Klooster, S. A.: Terrestrial ecosystem production: a process model based on global satellite and surface data, Glob. Biogeochem. Cy., 7, 811–841, 1993. 15130

Raich, J. W. and Schlesinger, W. H.: The global carbon dioxide flux in soil respiration and its relationship to vegetation and climate, Tellus B, 44, 81–99, 1992. 15130

Raich, J. W., Potter, C. S., and Bhagawati, D.: Interannual variability in global soil respiration, 1980-94, Global Change Biol., 8, 800–812, 2002. 15136

Randerson, J. T., Thompson, M. V., Malmstrm̈, C. M., Field, C. B., and Fung, I. Y.: Substrate limitations for heterotrophs: Implications for models that estimate the seasonal cycle of atmospheric CO_2, Glob. Biogeochem. Cy., 10, 585–602, doi:10.1029/96GB01981, 1996. 15134

Rayner, P. J., Scholze, M., Knorr, W., Kaminski, T., Giering, R., and Widmann, H.: Two decades of terrestrial carbon fluxes from a carbon cycle data assimilation system (CCDAS), Glob. Biogeochem. Cy., 19, 20 pp., doi:10.1029/2004GB002254, 2005. 15130, 15131

BGD
9, 15127–15174, 2012

Reichstein, M., Rey, A., Freibauer, A., Tenhunen, J., Valentini, R., Banza, J., Casals, P., Cheng, Y. F., Grünzweig, J. M., Irvine, J., Joffre, R., Law, B. E., Loustau, D., Miglietta, F., Oechel, W., Ourcival, J.-M., Pereira, J. S., Peressotti, A., Ponti, F., Qi, Y., Rambal, S., Rayment, M., Romanya, J., Rossi, F., Tedeschi, V., Tirone, G., Xu, M., and Yakir, D.: Modeling temporal and large-scale spatial variability of soil respiration from soil water availability, temperature and vegetation productivity indices, Glob. Biogeochem. Cy., 17, 1104, doi:10.1029/2003GB002035, 2003. 15128, 15130, 15136, 15137, 15138, 15142

Reichstein, M., Kätterer, T., Andrén, O., Ciais, P., Schulze, E.-D., Cramer, W., Papale, D., and Valentini, R.: Temperature sensitivity of decomposition in relation to soil organic matter pools: critique and outlook, Biogeosciences, 2, 317–321, doi:10.5194/bg-2-317-2005, 2005. 15130

Rödenbeck, C.: Estimating CO_2 sources and sinks from atmospheric mixing ratio measurements using a global inversion of atmospheric transport, Tech. Rep. 6, Max Planck Institute for Biogeochemistry, Jena, Germany, 2005. 15138, 15139, 15148, 15166, 15167, 15168, 15169, 15170

Rödenbeck, C., Houweling, S., Gloor, M., and Heimann, M.: CO_2 flux history 1982–2001 inferred from atmospheric data using a global inversion of atmospheric transport, Atmos. Chem. Phys., 3, 1919–1964, doi:10.5194/acp-3-1919-2003, 2003. 15129

Running, S. W., Nemani, R. R., Glassy, J. M., and Thornton, P. E.: MODIS Daily Photosynthesis (PSN) and Annual Net Primary Production (NPP) Product (MOD17), Tech. rep., NASA, 1999. 15135

Running, S. W., Nemani, R. R., Heinsch, F. A., Zhao, M. S., Reeves, M., and Hashimoto, H.: A continuous satellite-derived measure of global terrestrial primary production, Bioscience, 54, 547–560, 2004. 15135, 15143

Scholze, M., Kaplan, J. O., Knorr, W., and Heimann, M.: Climate and interannual variability of the atmosphere-biosphere $13CO_2$ flux, Geophys. Res. Lett., 30, 4 pp., doi:10.1029/2002GL015631, 2003. 15131

Schwalm, C., Williams, C. A., Schaefer, K., Anderson, R., Arain, M. A., Baker, I., Barr, A., Black, T. A., Chen, G. S., Chen, J. M., Ciais, P., Davis, K. J., Desai, A., Dietze, M., Dragoni, D., Fischer, M. L., Flanagan, L. B., Grant, R., Gu, L. H., Hollinger, D., Izaurralde, R. C., Kucharik, C., Lafleur, P. M., Law, B. E., Li, L. H., Li, Z. P., Liu, S. G., Lokupitiya, E., Luo, Y. Q., Ma, S. Y., Margolis, H., Matamala, R., McCaughey, H., Monson, R. K., Oechel, W. C., Peng, C. H., Poulter, B., Price, D. T., Riciutto, D. M., Riley, W., Sahoo, A. K., Sprintsin, M., Sun, J. F., Tian, H. Q., Tonitto, C., Verbeeck, H., and Verma, S. B.: A model-data intercomparison

BGD
9, 15127–15174, 2012

of CO_2 exchange across North America: Results from the North American Carbon Program site synthesis, J. Geophys. Res., 115, 22 pp., doi:10.1029/2009JG001229, 2010. 15130
Sellers, P. J.: Canopy reflectance, photosynthesis and transpiration, Int. J. Remote Sens., 6, 1335–1372, 1985. 15132
Sellers, P. J., Los, S. O., Tucker, C. J., Justice, C. O., Dazlich, D. A., Collatz, G. J., and Randall, D. A.: A revised land surface parameterization (SiB2) for atmospheric GCMs. Part II: The generation of global fields of terrestrial biophysical parameters from satellite data, J. Climate, 9, 706–737, 1996a. 15148
Sellers, P. J., Randall, D. A., Collatz, G. J., Berry, J. A., Field, C. B., Dazlich, D. A., Zhang, C., Collelo, C. D., and Bounoua, L.: A revised land surface parameterization (SiB2) for atmospheric GCMs: Part 1. Model formulation, J. Climate, 9, 676–705, 1996b. 15134
Sitch, S., Huntingford, C., Gedney, N., Levy, P., Lomas, M., Piao, S., Betts, R., Ciais, P., Cox, P., Friedlingstein, P., Jones, C. D., Prentice, I. C., and Woodward, F. I.: Evaluation of the terrestrial carbon cycle, future plant geography and climate-carbon cycle feedbacks using five Dynamic Global Vegetation Models (DGVMs), Global Change Biol., 14, 2015–2039, 2008. 15130
Stephenson, N. L.: Climatic control of vegetation distribution: the role of the water balance, The American Naturalist, 135, 649–670, 1990. 15143
Thornton, P. E., Running, S. W., and Hunt, E. R.: Biome-BGC: Terrestrial Ecosystem Process Model, Version 4.1.1. Data model, Oak Ridge National Laboratory Distributed Active Archive Center, Oak Ridge, Tennessee, USA, available at: http://www.daac.ornl.gov, last access: December 2010, 2005. 15139
Trusilova, K. and Churkina, G.: The terrestrial ecosystem model BIOME-BGC v1, Tech. Rep. 14, MPI BGC, Jena (Germany), 2008. 15139
Trusilova, K., Trembath, J., and Churkina, G.: Parameter estimation and validation of the terrestrial ecosystem model BIOME-BGC using eddy-covariance flux measurments, Tech. Rep. 16, MPI BGC, Jena, Germany, 2009. 15152
Tucker, C. J., Pinzon, J. E., Brown, M. E., Slayback, D., Pak, E. W., Mahoney, R., Vermote, E. F., and Saleous, N. E.: An Extended AVHRR 8-km NDVI Data Set Compatible with MODIS and SPOT Vegetation NDVI Data, Int. J. Remote Sens., 26, 4485–5598, 2005. 15133, 15139, 15140
Valentini, R., Matteucci, G., Dolman, A. J., Schulze, E.-D., Rebmann, C., Moors, E. J., Granier, A., Gross, P., Jensen, N. O., Pilegaard, K., Lindroth, A., Grelle, A., Bernhofer, C., Grünwald,

BGD
9, 15127–15174, 2012

T., Aubinet, M., Ceulemans, R., Kowalski, A. S., Vesala, T., Rannik, Ü., Berbigier, P., Loustau, D., Guomundsson, J., Thorgeirsson, H., Ibrom, A., Morgenstern, K., Clement, R., Moncrieff, J., Montagnani, L., Minerbi, S., and Jarvis, P. G.: Respiration as the main determinant of carbon balance in European forests, Nature, 404, 861–865, 2000. 15143

van der Werf, G. R., Randerson, J. T., Collatz, G. J., Giglio, L., Kasibhatla, P., Arellano, A., Olsen, S. C., and Kasischke, E. S.: Continental-scale partitioning of fire emissions during the 1997 to 2001 El Nino/La Nina period, Science, 303, 73–76, 2004. 15134

Wang, T., Ciais, P., Piao, S. L., Ottlé, C., Brender, P., Maignan, F., Arain, A., Cescatti, A., Gianelle, D., Gough, C., Gu, L., Lafleur, P., Laurila, T., Marcolla, B., Margolis, H., Montagnani, L., Moors, E., Saigusa, N., Vesala, T., Wohlfahrt, G., Koven, C., Black, A., Dellwik, E., Don, A., Hollinger, D., Knohl, A., Monson, R., Munger, J., Suyker, A., Varlagin, A., and Verma, S.: Controls on winter ecosystem respiration in temperate and boreal ecosystems, Biogeosciences, 8, 2009–2025, doi:10.5194/bg-8-2009-2011, 2011. 15143, 15146

BGD
9, 15127–15174, 2012

Table 1. SYNMAP (Jung et al., 2006) land cover classification and its aggregation into seven major PFTs. See Table 2 for the descriptive abbreviations used for the PFTs.

	SYNMAP (Jung et al., 2006)			7 major PFT's
Class	Life forms	Tree leaf type	Tree leaf longevity	PFT(index)
1	Trees	Needle	Evergreen	ENF (1)
2	Trees	Needle	Deciduous	DxF (3)
3	Trees	Needle	Mixed	DxF (3)
4	Trees	Broad	Evergreen	EBF (2)
5	Trees	Broad	Deciduous	DxF (3)
6	Trees	Broad	Mixed	DxF (3)
7	Trees	Mixed	Evergreen	DxF (3)
8	Trees	Mixed	Deciduous	DxF (3)
9	Trees	Mixed	Mixed	DxF (3)
10	Trees and Shrubs	Needle	Evergreen	ENF (1)
11	Trees and Shrubs	Needle	Deciduous	DxF (3)
12	Trees and Shrubs	Needle	Mixed	DxF (3)
13	Trees and Shrubs	Broad	Evergreen	SAV (5)
14	Trees and Shrubs	Broad	Deciduous	SAV (5)
15	Trees and Shrubs	Broad	Mixed	SAV (5)
16	Trees and Shrubs	Mixed	Evergreen	SAV (5)
17	Trees and Shrubs	Mixed	Deciduous	SAV (5)
18	Trees and Shrubs	Mixed	Mixed	DxF (3)
19	Trees and Grasses	Needle	Evergreen	ENF (1)
20	Trees and Grasses	Needle	Deciduous	DxF (3)
21	Trees and Grasses	Needle	Mixed	DxF (3)
22	Trees and Grasses	Broad	Evergreen	EBF (2)
23	Trees and Grasses	Broad	Deciduous	SAV (5)
24	Trees and Grasses	Broad	Mixed	SAV (5)
25	Trees and Grasses	Mixed	Evergreen	DxF (3)
26	Trees and Grasses	Mixed	Deciduous	DxF (3)
27	Trees and Grasses	Mixed	Mixed	SAV (5)
28	Trees and Crops	Needle	Evergreen	CRO (7)
29	Trees and Crops	Needle	Deciduous	CRO (7)
30	Trees and Crops	Needle	Mixed	CRO (7)
31	Trees and Crops	Broad	Evergreen	CRO (7)
32	Trees and Crops	Broad	Deciduous	CRO (7)
33	Trees and Crops	Broad	Mixed	CRO (7)
34	Trees and Crops	Mixed	Evergreen	CRO (7)
35	Trees and Crops	Mixed	Deciduous	CRO (7)
36	Trees and Crops	Mixed	Mixed	CRO (7)
37	Shrubs	–	–	SHR (4)
38	Shrubs and Grasses	–	–	SHR (4)
39	Shrubs and Crops	–	–	SHR (4)
40	Shrubs and Barren	–	–	SHR (4)
41	Grasses	–	–	GRS (6)
42	Grasses and Crops	–	–	GRS (6)
43	Grasses and Barren	–	–	GRS (6)
44	Crops	–	–	CRO (7)
45	Barren	–	–	(ignored) (8)
46	Urban	–	–	(ignored) (8)
47	Snow and Ice	–	–	(ignored) (8)

BGD
9, 15127–15174, 2012

Table 2. Descriptive abbreviations used for PFTs and the values of PFT-dependent parameters of the photosynthesis model. ε_{max}: maximum light use efficiency per PFT, $T_{min,1\,PFT}$: the daily minimum temperature at which $\varepsilon = 0.0$ (at any VPD), $VPD_{1\,PFT}$: the daylight average vapor pressure deficit at which $\varepsilon = 0.0$ (at any T_{min}), $VPD_{0\,PFT}$: the daylight average vapor pressure deficit at which $\varepsilon = \varepsilon_{max}$ (for optimal T_{min}).

Abbreviation (index)	Class full name	ε_{PFT} ($gC\,MJ^{-1}$)	$T_{min,1\,PFT}$ (°C)	VPD_1 PFT (Pa)	VPD_0 PFT (Pa)
ENF (1)	Evergreen needle	1.0	8.3	650	3100
EBF (2)	Evergreen broadleaf	1.0	9.1	1100	3600
DxF (3)	Deciduous/mixed forest	1.2	9.5	935	3350
SHR (4)	Shrubland	0.8	8.7	970	4100
SAV (5)	Savanna	0.8	11.4	1100	5000
GRS (6)	Grassland	0.6	12.0	1000	5000
CRO (7)	Cropland	1.1	12.0	930	4100

BGD
9, 15127–15174, 2012

Table 3. Climatic contributions to the interannual variability of GPP and R_{eco} over different land regions. The contribution was calculated using Eq. (15) and (16).

	GPP			R_{eco}	
Land Regions	VPD	Radiation	Temperature	Precipitation	Temperature
Land Total	0.43	0.39	0.18	0.32	0.68
Northern Hemisphere	0.47	0.10	0.43	0.13	0.87
Tropical Land	0.44	0.56	0.00	0.51	0.49
Southern Hemisphere	0.89	0.09	0.02	0.83	0.17
North American Bor.	0.17	0.05	0.77	0.02	0.98
North American Temp.	0.77	0.14	0.09	0.40	0.60
South American Trop.	0.46	0.53	0.00	0.74	0.26
South American Temp.	0.76	0.21	0.03	0.68	0.32
Europe	0.56	0.17	0.27	0.14	0.86
Northern Africa	0.58	0.42	0.00	0.62	0.38
Southern Africa	0.76	0.24	0.00	0.91	0.09
Eurasian Boreal	0.28	0.10	0.63	0.10	0.90
Eurasian Temperate	0.53	0.34	0.13	0.45	0.55
Tropical Asia	0.11	0.89	0.00	0.55	0.45
Australia	0.91	0.09	0.01	0.88	0.12

BGD
9, 15127–15174, 2012

Table 4. Lower (2nd) and upper (98th) NDVI percentiles estimated per PFT.

PFT(class)	$NDVI_{min}$	$NDVI_{max}$
ENF (1)	0	0.83
EBF (2)	0	0.90
DxF (3)	0	0.85
SHR (4)	0	0.75
SAV (5)	0	0.81
GRS (6)	0	0.74
CRO (7)	0	0.80

BGD
9, 15127–15174, 2012

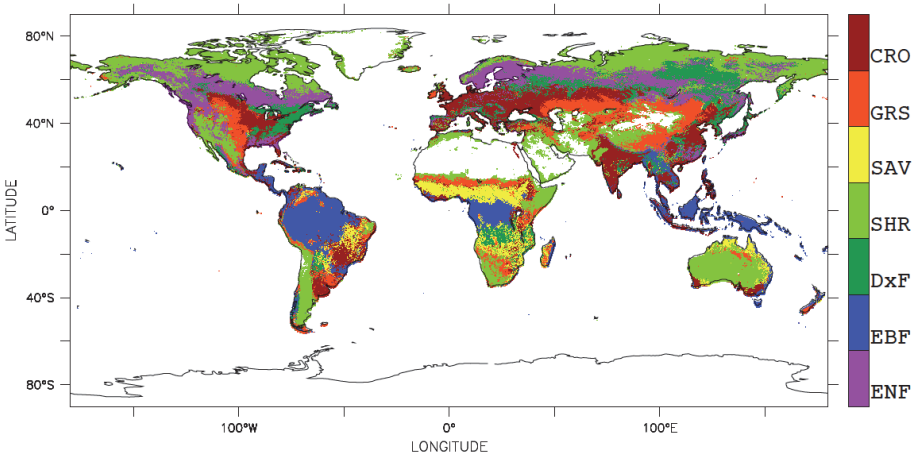

Fig. 1. The SYNMAP (Jung et al., 2006) land cover dataset aggregated into seven major PFTs in the GIMMS NDVI grid (8 km × 8 km) (see Table 1). PFT labels are described in Table 2. The Fractional cover map for each PFT with a spatial resolution of 4° latitude × 5° longitude are shown if Fig. 10.

BGD
9, 15127–15174, 2012

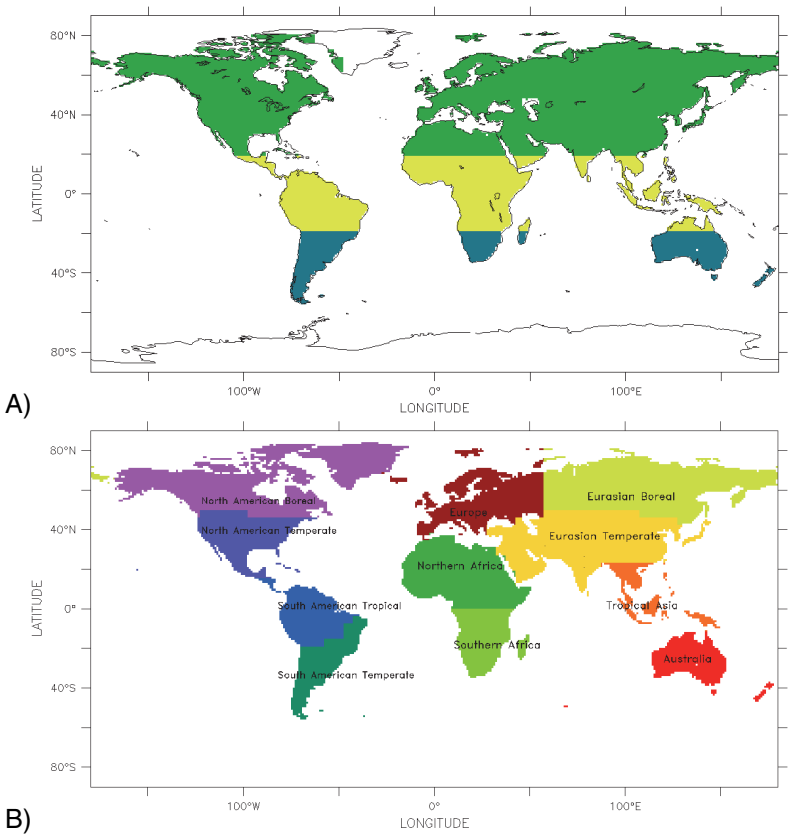

Fig. 2. Map of the land regions over which the estimated fluxes are integrated to obtain time series. **(A)** Land regions for three latitudinal bands defined as (90° S–20° S, 20° S–20° N and 20° N–90° N). **(B)** Land regions as defined in the TransCom3 project (Gurney et al., 2002).

BGD
9, 15127–15174, 2012

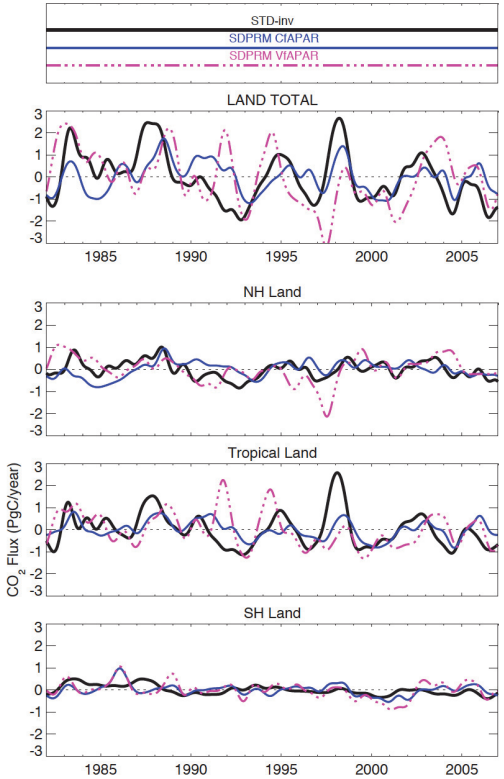

Fig. 3. The comparison between the anomaly (deviation from the mean of 1982–2006) of the IAV of the estimated NEE from SDPRM-CfAPAR (using the mean seasonal cycle of fAPAR) (blue) and SDPRM-VfAPAR (using the full variability of fAPAR) (magenta dashed) and the total land flux estimated by STD-inv (black). The time series are integrated over three latitudinal bands (for the map of the regions see Fig. 2) and de-seasonalized and filtered for interannual variability (as in Rödenbeck, 2005). The fossil fuel emissions have been subtracted for STD-inv line.

BGD
9, 15127–15174, 2012

Simple Diagnostic Photosynthesis and Respiration Model

B. Badawy et al.

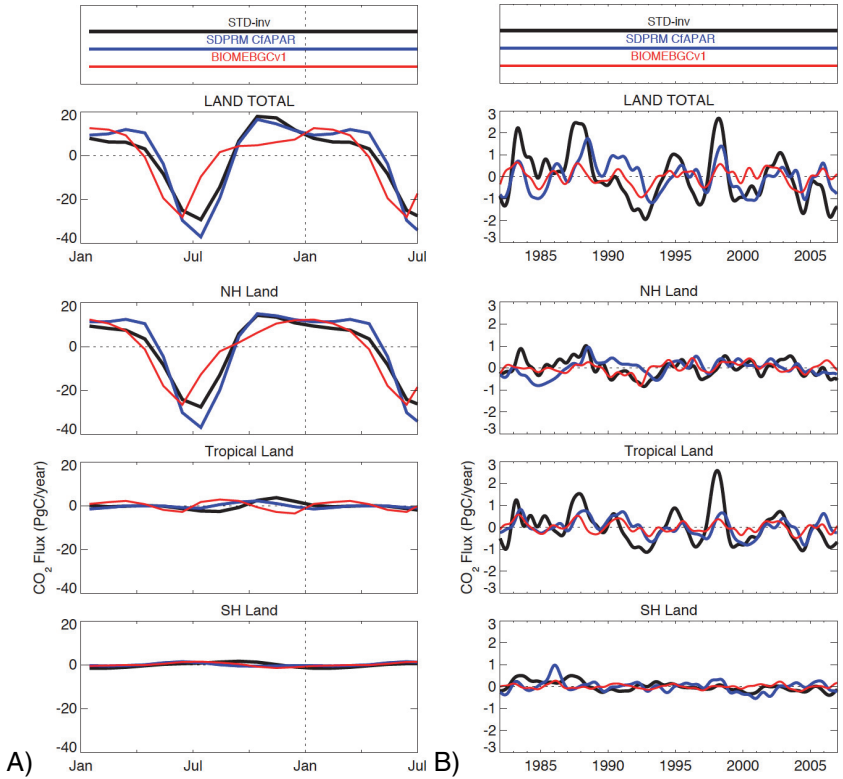

Fig. 4. The comparison between NEE estimates from SDPRM-CfAPAR (blue), BIOME-BGCv1 (red), and the land flux estimated by STD-inv (black) for the monthly mean seasonal cycle **(A)** and for the interannual variability **(B)**. The time series are integrated over three latitudinal bands (for the map of the regions see Fig. 2) and de-seasonalized and filtered for interannual variability (as in Rödenbeck, 2005). The fossil fuel emissions have been subtracted from STD-inv line.

BGD
9, 15127–15174, 2012

Simple Diagnostic Photosynthesis and Respiration Model

B. Badawy et al.

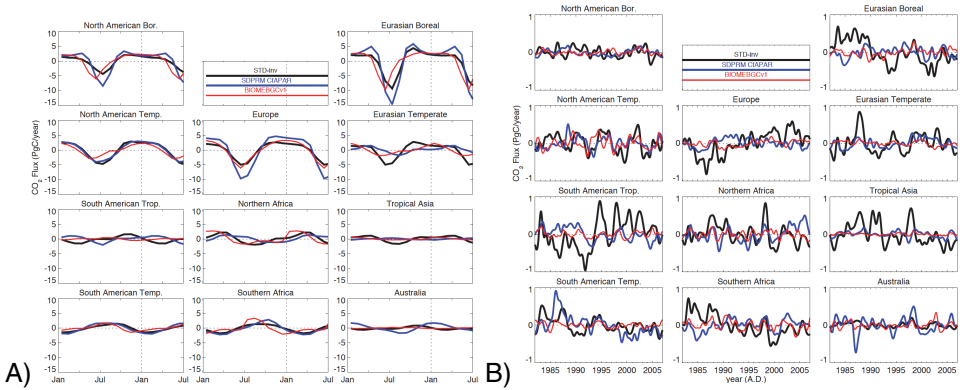

Fig. 5. The comparison between the estimated NEE from SDPRM-CfAPAR [Blue], BIOME-BGCv1 [Red],and the land flux estimated by STD-inv [Black] for the monthly mean seasonal cycle **(A)** and for the interannual variability **(B)**. The time series are integrated over 11 land regions (for the map of the regions see Fig. 2) and de-seasonalized and filtered for interannual variability (as in Rödenbeck, 2005). The fossil fuel emissions have been subtracted from STD-inv line.

BGD
9, 15127–15174, 2012

Simple Diagnostic Photosynthesis and Respiration Model

B. Badawy et al.

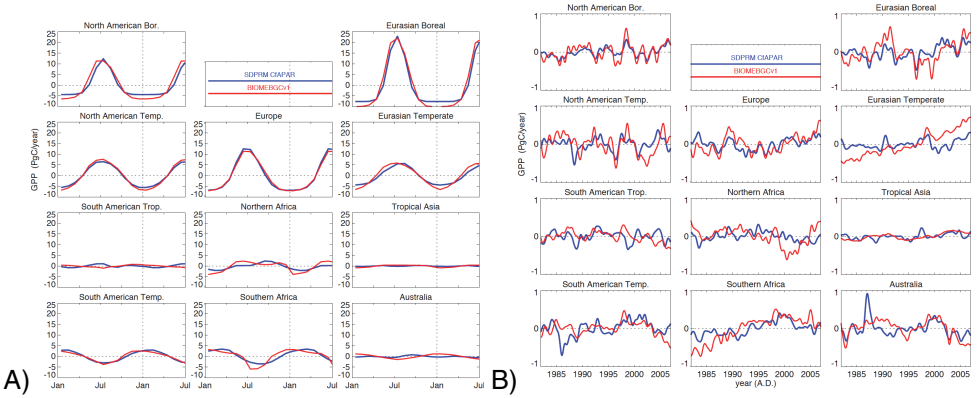

Fig. 6. The comparison between the estimated GPP from SDPRM-CfAPAR (Blue), and from BIOME-BGCv1 (Red) for the monthly mean seasonal cycle **(A)** and for the interannual variability **(B)**. The time series are integrated over 11 land regions (for the map of the regions see Fig. 2) and de-seasonalized and filtered for interannual variability (as in Rödenbeck, 2005).

BGD
9, 15127–15174, 2012

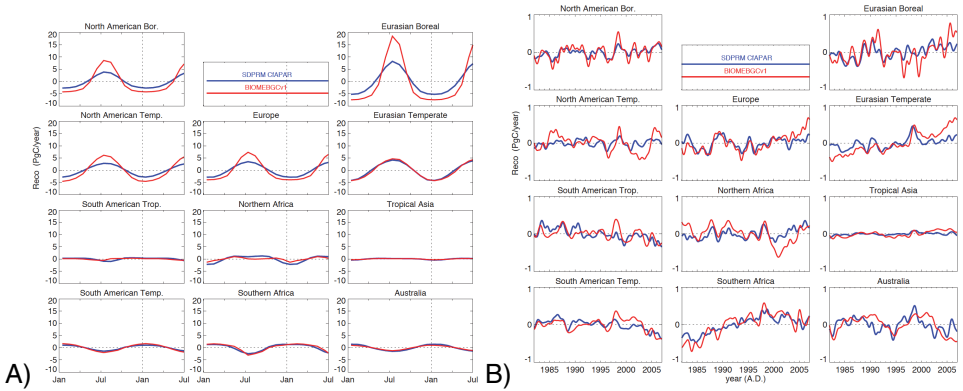

Fig. 7. The comparison between the estimated R_{eco} from SDPRM-CfAPAR (Blue), and from BIOME-BGCv1 (Red) for the monthly mean seasonal cycle **(A)** and for the interannual variability **(B)**. The time series are integrated over 11 land regions (for the map of the regions see Fig. 2) and de-seasonalized and filtered for interannual variability (as in Rödenbeck, 2005).

BGD
9, 15127–15174, 2012

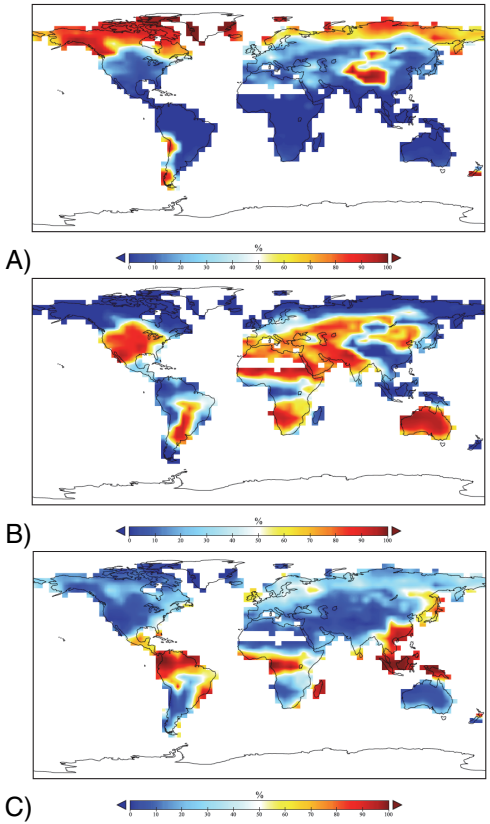

Fig. 8. The global distribution of the relative contribution of each climate variable (**(A)** temperature: high values indicate LOW temperature is limiting, **(B)** vapor pressure deficit (VPD): high value indicate HIGH VPD is limiting, and **(C)** radiation: high value indicate high LOW radiation is limiting) to the interannual variability (IAV) of GPP.

BGD
9, 15127–15174, 2012

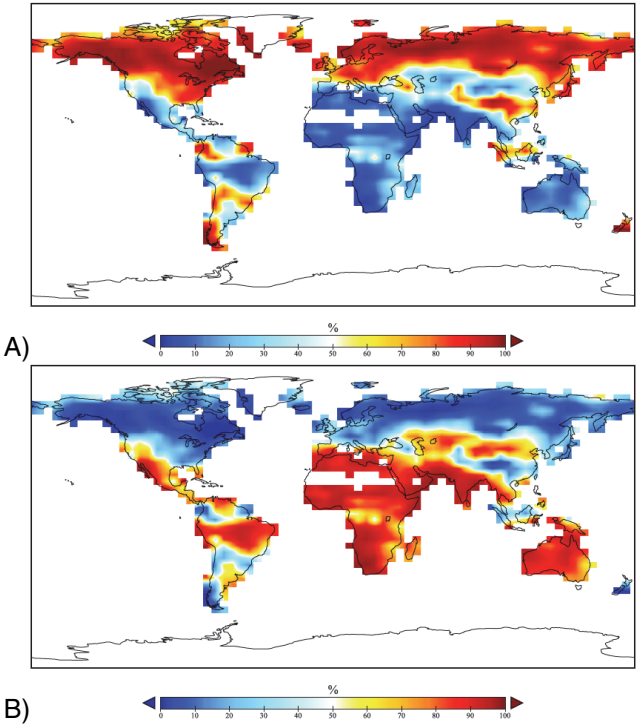

Fig. 9. The global distribution of the relative contribution of each climate variable (**(A)** temperature: high values indicate LOW temperature is limiting, **(B)** precipitation: high values indicate LOW precipitation is limiting) to the interannual variability (IAV) of R_{eco}.

BGD
9, 15127–15174, 2012

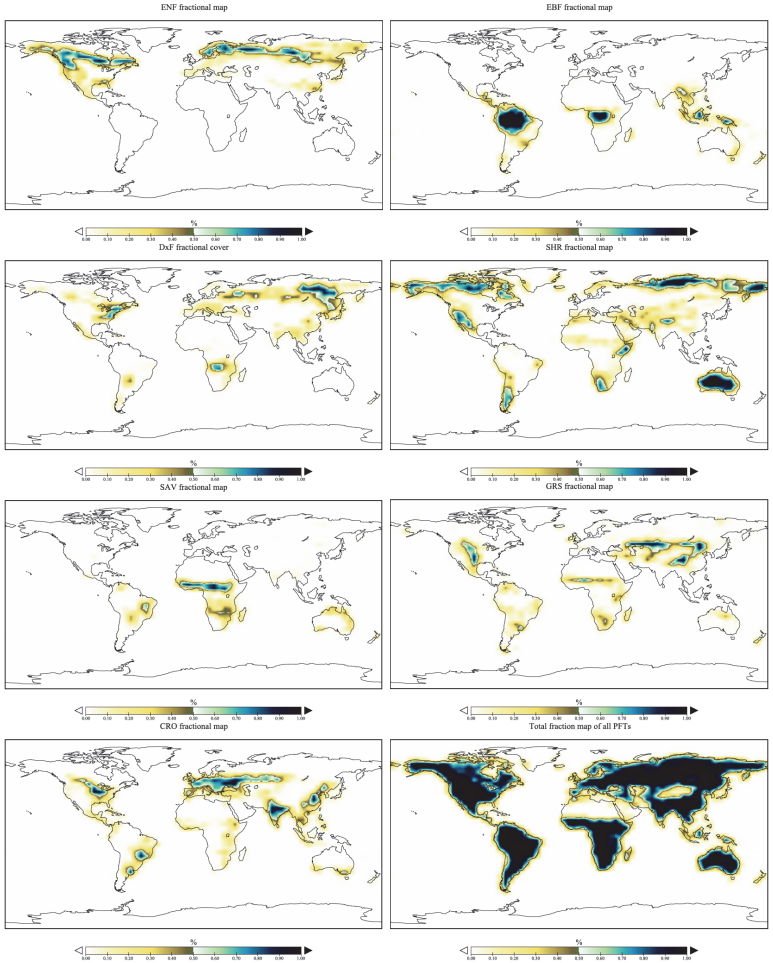

Fig. 10. Fractional cover map for each Plant Function Type PFT with a spatial resolution of 4° latitude × 5° longitude. The total fractional cover of PFTs is shown in the lower right panel.

BGD
9, 15127–15174, 2012

Simple Diagnostic Photosynthesis and Respiration Model

B. Badawy et al.

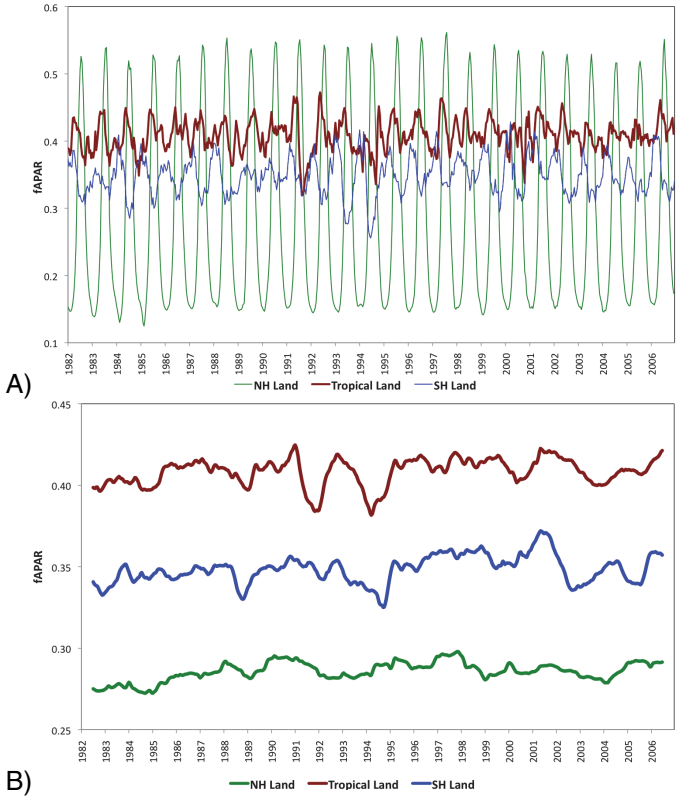

Fig. 11. Integrated fAPAR time series calculated from GIMMS NDVI across three latitudinal bands: **(A)** time series of the full temporal variability of fAPAR, **(B)** time series of the running annual average (box-car filter) of fAPAR. For a map of the regions see Fig. 2.

BGD
9, 15127–15174, 2012